PHYSICAL REVIEW B **108**, L140302 (2023)

Letter

Nonperturbative determination of isotope-induced anomalous vibrational physics

Huan Wu,[1] Zihao Qin,[1] Suixuan Li,[1] Lucas Lindsay,[2] and Yongjie Hu[1,*]
[1]*School of Engineering and Applied Science, University of California, Los Angeles, Los Angeles, California 90095, USA*
[2]*Materials Science and Technology Division, Oak Ridge National Laboratory, Oak Ridge, Tennessee 37831, USA*

(Received 30 July 2021; revised 24 June 2023; accepted 29 August 2023; published 18 October 2023;
corrected 6 November 2023)

In general, vibrational physics has been well described by quantum perturbation theory (QPT) to provide footprint characteristics for common crystals. However, despite weak phonon anharmonicity, the recently discovered cubic crystals (BAs and BP) have shown anomalous vibrational dynamics with elusive fundamental origin. Here, we developed a nonperturbative *ab initio* approach, together with spectroscopy and high-pressure experiments, to successfully determine the exact dynamic evolutions of the vibrational physics. We found that the local fluctuation and coupling isotopes significantly dictate the vibrational spectra, through the Brillouin zone folding that has previously been ignored in literature. By decomposing vibrational spectra into individual isotope eigenvectors, we observed both positive and negative contributions to Raman intensity from constitutional atoms (^{10}B, ^{11}B, ^{75}As, or ^{31}P). Importantly, our nonperturbative theory predicts that a vibrational resonance appears at high hydrostatic pressure due to broken translational symmetry, which was indeed verified by experimental measurement under a pressure up to 31.5 GPa. In this paper, we develop fundamental understandings for the anomalous lattice physics under the failure of QPT and provide an approach in exploring transport phenomena for materials of extreme properties.

DOI: 10.1103/PhysRevB.108.L140302

Quantum perturbation theory (QPT) is a general approach to describe quantum systems involving phonon, photon, or electron interactions [1,2]. The idea of QPT is to start with a simple system that can be easily solved and then add a perturbing Hamiltonian representing a weak disturbance to the system. The complicated systems can therefore be studied based on the knowledge of the simpler one [3,4]. So far, exceptions to QPT only exist in complicated or extreme systems of strong correlations, confinement, anharmonicity, interactions, or bound states [5–20]. For most crystals, the vibrational physics can be well characterized by perturbation theory and thus provide footprint features of their crystal structures [21–23]. However, here, we found that, in the recently discovered cubic crystals, boron arsenide (BAs) and boron phosphide (BP), the coupling and random distribution of isotope atoms breaks the translational symmetry and folds the Brillouin zone; thus, the vibration energy cannot be described by perturbation theory [24–30]. To understand the missing phonon physics, we developed a nonperturbative *ab initio* approach to accurately construct the vibrational spectra and enable deterministic predictions matching experimental measurements under controlled isotopes and high pressure.

In the literature, QPT has been well applied for simulating vibrational spectra and shown good agreement with experiments for common materials including diamond, Si, Ge, GaAs, InP, AlP, AlSb, AlAs, GaSb, InAs, InSb, SiC, BN, AlN, and GaN [21–23,31–64]. In general, each Raman peak is dictated by the vibrational energy corresponding to a phonon branch. However, the recently discovered BAs [24,26–30,64–68] and BP [25] exhibit anomalous Raman spectra evolving between single and two modes with isotope stochastic ratio, which does not follow the established understanding and has puzzled the field for the last several years. Based on the conventional understanding, authors of early studies mistakenly attributed the two Raman peaks to the longitudinal optical (LO) and transverse optical (TO) modes, which was later found to be incorrect because the LO-TO splitting is too small in energy to be observable [25,30,69,70]. Later on, the two modes were naively assigned to isotope vibrations (^{10}B and ^{11}B) simply due to energy proximity, but the fundamental origin is not clear, and the measurement remains inconsistent with theory [27,30]. Further experiments [71,72] with tailored isotopes measured the abnormal Raman profiles with transition from single- to two-mode behaviors as a function of isotope stoichiometries, which indicates the isotope disorder is important but can no longer be treated perturbatively. So far, such an anomalous two-mode behavior has not been seen in any other cubic crystals [22]. In the following, we will start by elaborating established models and missing physics in the past literature and then proceed to discuss our development that enables quantitative understanding of the vibrational dynamics.

Many authors of prior studies have considered the disorder effects through QPT [3,4], e.g., treating the isotope interactions as perturbation to a periodic system. Using a mean field perturbation, the eigenmodes or scattering rates can be derived. Under the weak scattering limit, phonon interactions with defects (including isotopes) can be derived from Fermi's golden rule [73] and show good agreement with the measured phonon linewidths [22]. For increased isotope interactions, the phonon frequency shift due to renormalization can be derived by improving QPT with perturbative quantum field

---

[*] yhu@seas.ucla.edu

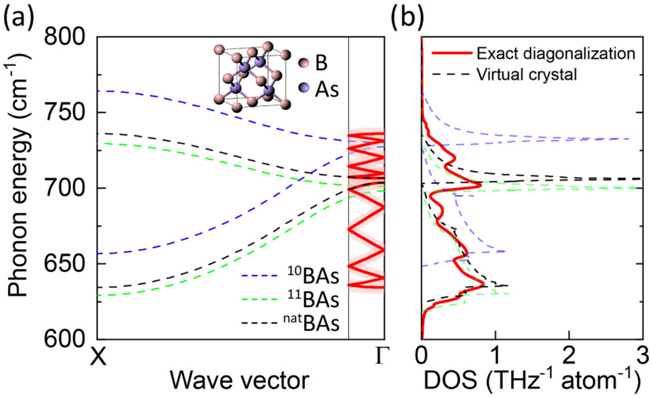

FIG. 1. Brillouin zone folding and translational symmetry breaking due to local disorder and coupling of distributed isotope atoms. (a) Phonon band structures (optic branches) for isotopically pure and naturally abundant BAs. Schematic in the right column (red shadow) illustrating an example of Brillouin zone folding due to local and coupled isotope effects. (b) Phonon density of states (DOS) calculated by different model methods. The DOS of naturally abundant BAs is determined by the supercell exact diagonalization theory (red solid curve) to include the prior missing contributions from local isotope disorders and their coupling, showing clear differences from the virtual crystal calculation (black dashed curve). The comparison indicates a substantial redistribution of phonon states due to isotope effects of Brillouin zone folding and energy splitting.

theory [74]. However, fundamentally, all the above perturbative theory frameworks were found to be inadequate for BAs and BP due to their unique atomic structures. We attribute this to two essential missing factors: First, local disorder from randomly distributed isotope atoms can be critical and break the lattice translational symmetry. Second, the coupling interactions between isotope atoms with relatively large mass difference (such as ^{11}B and ^{10}B in BAs or BP) will enable a nonnegligible energy splitting for optical phonon modes and thus substantially revise the Hamiltonian from the statistical average or mean field approximation in QPT.

Here, to capture the localized and coupling isotopic vibrational physics in BAs and BP, we develop an *ab initio* approach based on nonperturbative supercell exact diagonalization [75,76] and density functional theory (DFT) [77,78]. First, we consider the scattering physics of localized isotope disorders as effective folding of the Brillouin zone: In a perfect crystal, atoms are arranged as periodic repetitions of a primitive cell, while for a practical crystal with a mixture of isotopes, isotope atoms could distribute randomly in space and thus form local disorders to break the original periodicity. Effectively, we treat such a disorder effect as to enlarge the lattice periodicity and fold the Brillouin zone, i.e., additional phonon states will be projected to the Γ point and become assessable for Raman scattering. An exemplary Brillouin zone folding picture is schematically illustrated by the pink shadowed curves in Fig. 1(a). Second, we explicitly consider the coupling effects from all individual isotope atoms (e.g., ^{10}B, ^{11}B, ^{75}As, ^{31}P) by computing the exact eigenstates from a randomly configured supercell. The importance of such a coupling effect in BAs can be gauged from our calculated phonon dispersions for isotopically purely crystals (blue and green dashed curves) in Fig. 1(a): The energy level splitting between ^{10}BAs and ^{11}BAs is larger than that observed in common compounds and phonon linewidths; thus, as we expected, the isotope interactions should play an important role in reshaping the vibration spectra. To capture both missing factors from the localized and coupling isotope effects, we form a large supercell with randomly assigned mass for each atom based on isotope concentrations and then directly diagonalize the dynamical matrix of the supercell to determine the eigenfrequencies and eigenvectors that capture the exact isotope interactions [79]. The exact eigenfrequencies of the disordered system are obtained nonperturbatively to include energy splitting. The interatomic force constants are determined by the *ab initio* approach [80,81] based on DFT [77,78] without using fitting parameters or empirical potentials. To ensure an accurate calculation on long-range interatomic interactions within a large supercell, we employ nonlocal density functionals [82–86] in DFT calculations using QUANTUM ESPRESSSO [87–89]. The interatomic force constants are subsequently extracted by fitting the displacement-force sets using ALAMODE [90]. The dipole-dipole interactions are considered through a mixed-space approach [91]. We randomly generated 1000 mass configurations on a supercell of 512 atoms while keeping the interatomic potential same. The final density of states (DOS) spectra is derived by averaging over the spectra of those mass configurations. Since each mass configuration represents a local snapshot of disorder, the Brillouin zone folding due to translational symmetry breaking is fully considered with a large supercell and multilattice repetitions. Figure 1(b) shows the phonon DOS calculated by our nonperturbative supercell exact diagonalization method (red curves) in comparison with virtual crystal approximation (dashed curves): Clearly, a large deviation is observed between the two methods for naturally abundant BAs, verifying our hypothesis that isotope coupling and disorder-induced zone folding substantially modulate the phonon states.

Next, to determine the exact profile of Raman spectra, we looked at its basic physical process: In a Raman experiment, electrons are the medium of photon-phonon interaction. Under laser, electrons will oscillate with the external electromagnetic wave, which induces an instantaneous polarization quantified by electrical dipole moment $P^{\mu} = \boldsymbol{\alpha}^{\mu\nu} E^{\nu}$, where $\boldsymbol{E}$ is the electric field, $\boldsymbol{\alpha}$ is the polarizability tensor, and μ and ν indicate direction. The light intensity $I(\omega)$ is proportional to the square of the electromagnetic wave amplitude:

$$I(\omega) \propto |\hat{\boldsymbol{\varepsilon}}_S \cdot \boldsymbol{\alpha}(\omega) \cdot \hat{\boldsymbol{\varepsilon}}_I|^2, \tag{1}$$

where $\hat{\boldsymbol{\varepsilon}}_I$ and $\hat{\boldsymbol{\varepsilon}}_S$ are polarization vectors of the incident and scattered light, respectively [92,93].

The polarizability tensor can then be expanded as a power series with respect to atomic displacement $\mathbf{u}(jl)$:

$$\alpha^{\mu\nu} = \alpha_0^{\mu\nu} + \alpha_1^{\mu\nu} + \cdots, \tag{2}$$

where $\alpha_0^{\mu\nu}$ = constant, and

$$\alpha_1^{\mu\nu} = \sum_{\xi} \sum_{jl} \frac{\partial \alpha^{\mu\nu}}{\partial \xi} u_{\xi}(jl), \tag{3}$$

where $\mathbf{u}(jl)$ is the atomic displacement of the jth atom in lth cell, and μ, ν, and ξ indicate the directions of the coordinate system. In Eq. (2), the first term corresponds to elastic scattering, and the second term is associated with inelastic scattering due to electron-phonon interactions which contribute to the Raman spectra.

The atomic displacement $\mathbf{u}(jl)$ can be treated as the superposition of different modes of lattice waves:

$$\mathbf{u}(jl) = \frac{1}{\sqrt{Nm_j}} \sum_{\mathbf{q}s} \mathbf{e}_{\mathbf{q}s}(j)\exp[i\mathbf{q}\cdot\mathbf{r}(jl)]Q_{\mathbf{q}s}, \tag{4}$$

where $\mathbf{q}$ is the phonon wave vector, and s is the phonon branch; $\mathbf{q}s$ labels a certain phonon mode. Here, N is the number of $\mathbf{q}$ points in the first Brillouin zone, and m_j and $\mathbf{r}(jl)$ are, respectively, the mass and the equilibrium position of the jth atom in lth cell. Also, $Q_{\mathbf{q}s}$ is the normal mode coordinate and gives the amplitude of the lattice wave, and $\mathbf{e}_{\mathbf{q}s}(j)$ is the eigenvector of the jth atom. By substituting Eq. (4) into Eq. (3), $\boldsymbol{\alpha}_1$ can be expressed in terms of contributions from different phonon modes:

$$\alpha_1^{\mu\nu} = \sum_{\mathbf{q}\to 0,s} \frac{\partial \alpha^{\mu\nu}_{\mathbf{q}s}}{\partial Q_{\mathbf{q}s}} Q_{\mathbf{q}s}. \tag{5}$$

Here, only optical modes with $\mathbf{q} \to \mathbf{0}$ contribute to the Raman spectra due to the conservation of energy and momentum in photon-phonon interactions.

Consequently, the Raman intensity at a certain frequency ω is

$$I(\omega) \propto \sum_{s,\mathbf{q}\to 0} \frac{\left|\hat{\boldsymbol{\varepsilon}}_S\cdot \frac{\partial \boldsymbol{\alpha}_{\mathbf{q}s}}{\partial Q_{\mathbf{q}s}}\cdot\hat{\boldsymbol{\varepsilon}}_I\right|^2}{\omega_{\mathbf{q}s}}\delta(\omega-\omega_{\mathbf{q}s}). \tag{6}$$

For cubic crystals, the crystal symmetry dictates that $\partial\alpha_{\alpha\beta}/\partial u^{\gamma}_{jl} = at_j\epsilon_{\alpha\beta\gamma}$, where a is a constant, and $\epsilon_{\alpha\beta\gamma}$ represents the Levi-Civita symbol [94]. For binary compounds, $t_j = 1$ for anions, and $t_j = -1$ for cations. Hence,

$$\frac{\partial\alpha^{\mu\nu}}{\partial Q_{\mathbf{q}s}} = \sum_{jl}\frac{\partial\alpha^{\mu\nu}}{\partial\mathbf{u}_{jl}}\frac{\partial\mathbf{u}_{jl}}{\partial Q_{\mathbf{q}s}} \propto \sum_j t_j\epsilon_{\mu\nu\xi}\frac{\left(e^j_{\mathbf{q}s}\right)_\xi}{\sqrt{m_j}}. \tag{7}$$

When the incident and scattered light are along [111] orientation,

$$I(\omega) \propto \sum_{s,\mathbf{q}\to 0} \frac{\left|\sum_{j\xi} t_j\frac{(e^j_{\mathbf{q}s})_\xi}{\sqrt{m_j}}\right|^2}{\omega_{\mathbf{q}s}}\delta(\omega-\omega_{\mathbf{q}s}). \tag{8}$$

From Eq. (8), the Raman spectra is mainly determined by the phonon eigenvectors and phonon DOS.

Based on the above *ab initio* supercell exact diagonalization method, we determine the anomalous Raman spectra for BAs and BP varying with isotope concentrations (Fig. 2). To verify the calculation results, we chemically synthesized isotopically controlled BAs [27] and BP [25] crystals and performed the Raman measurements. The measured Raman spectra of BAs and BP were obtained from 633 nm wavelength laser excitation with 1200 mm^{-1} grating. We used the same laser power and spot size through all measurements in this paper to ensure that all samples are exposed under the same experimental conditions. Shown in Fig. 2(a), the Raman spectra by *ab initio* calculation (black dashed curve) are compared with experimental results from our measurement (red dots) and the literature [72] (red squares), all showing good agreement. The Raman peaks shift to higher frequency with increasing ^{10}B concentration, as the atoms tend to oscillate faster with smaller mass. The isotopically pure BAs and BP show only a single Raman peak but evolve to two modes under the coupling between different isotopes: For example, in naturally abundant BAs (i.e., with 20.1% ^{10}B concentration)

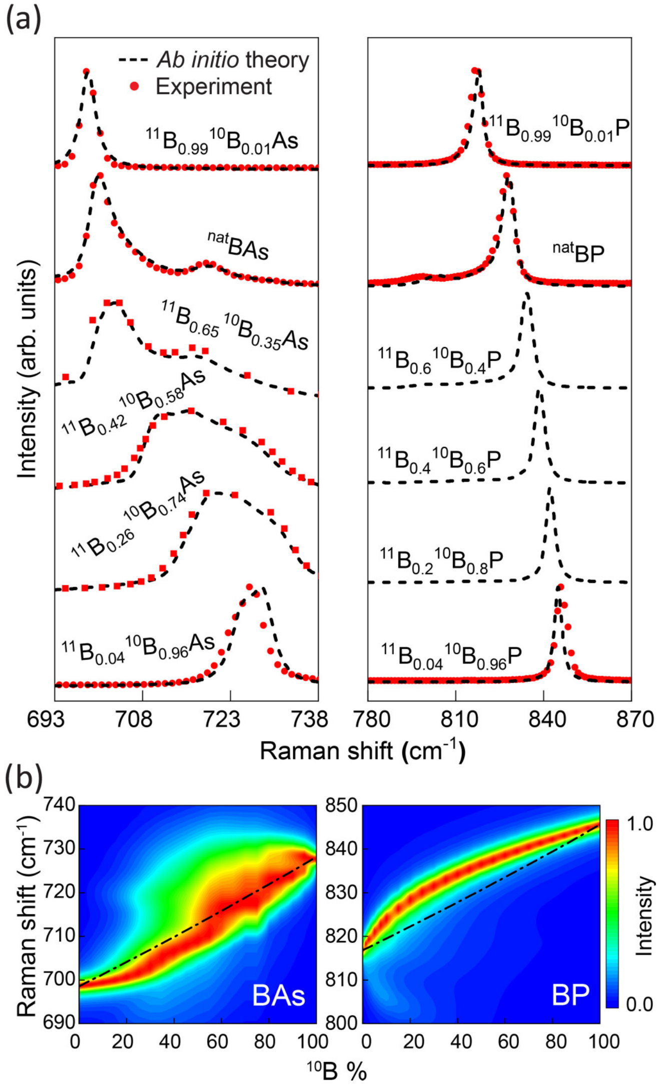

FIG. 2. Quantitative profile-determination of vibrational dynamics by *ab initio* theory in comparison with experimental measurements, under varying isotope concentrations. (a) The dynamic evolution of Raman spectra with different isotope stichometry concentrations between ^{10}B and ^{11}B for (a) BAs and (b) BP. The Raman spectral profiles determined by *ab initio* calculation based on the supercell exact diagonalization theory (black dashed curve), considering the local isotope disorder and their coupling, are in good agreement with experimental data from our measurement (red dot) and literature (red square) [72]. (b) The *ab initio* theory determined Raman spectra is plotted in a two-dimensional color map, illustrating the broadening of Raman spectra and evolution from single- to two-mode behaviors due to isotope coupling. Plotted for comparison is the virtual crystal approximation (dot-dashed curve), indicating its limitation to single mode and failure to capture the coupling physics in these boron compounds.

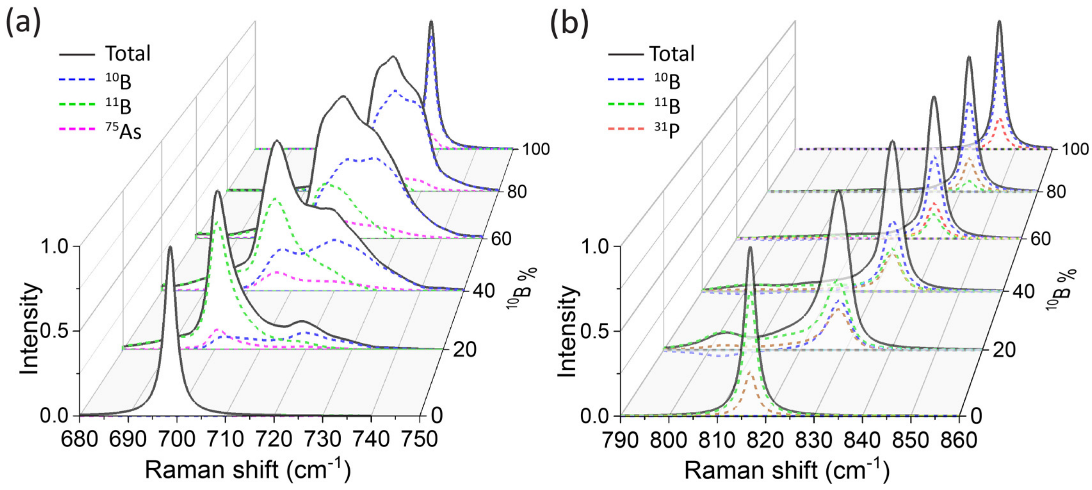

FIG. 3. Decomposition of vibrational spectra into constitutional atomic modes by tracing the eigenvectors. The Raman intensity for (a) BAs and (b) BP under varied isotope concentrations are decomposed into respective contributions of ^{10}B, ^{11}B, ^{75}As, or ^{31}P. The total Raman spectra (black solid curve) is a summation of all isotope contributions (dashed) and shows good agreement with experiments in Fig. 2. Negative contribution is observed from individual isotope mode, e.g., ^{10}B mode in $^{10}\mathrm{B}_{0.2}\,^{11}\mathrm{B}_{0.8}\,\mathrm{P}$.

[Fig. 2(a)], a second smaller peak appears at 718.9 cm^{-1} in addition to its first Raman peak at 700.8 cm^{-1}. With further increased concentration of $^{10}\mathrm{B} > 40\%$, the two peaks gradually move closer to each other and eventually merge when ^{10}B is $>80\%$. For BP, under the natural occurring boron isotope concentration, the second low-frequency Raman peak appears at 799.0 cm^{-1}, though with a smaller intensity of $\sim 10\%$ that of the first peak at 827.4 cm^{-1}. With increased ^{10}B concentration, the second peak gradually disappears. Based on our *ab initio* theory and their good agreement with experiment in Fig. 2(a), such an anomalous evolution of Raman spectra with isotope stoichiometries can be understood from Brillouin zone folding. In the Raman process, only the $\mathbf{q} = 0$ modes are active due to the energy and momentum conservation during photon-phonon interactions. For isotopically pure crystals where atomic masses are of perfect periodic distribution, the phonon mode at the Γ point forms a single Raman peak. Considering the extreme case, for example, in amorphous materials, disorders can destroy the periodicity or effectively project all vibrational modes following Brillouin zone folding; as a result, the Raman spectra of amorphous materials resemble the profile of DOS. In comparison, the isotope-mixed BAs and BP are mass disordered lattice with partial phonon modes folded to the Γ point and become accessible to Raman spectra. Further, we compare the results between the supercell exact diagonalization approach and the virtual crystal approximation. As shown in Fig. 2(b), the virtual crystal result (black dot-dashed curve) is always limited to a single Raman peak and is almost linearly changing with the ^{10}B fraction. Our *ab initio* results, on the other hand, show nonlinearity due to the evolutions from a single peak to two coupled peaks, consistent with the experimental observation. Essentially, the localized isotope vibrations and their coupling deviate from the calculations based on homogenous virtual atoms.

Importantly, in this paper, we indicate that each individual Raman peak involves substantial contributions from all isotope vibration modes, which means the respective Raman peak could be assigned to the separate vibrational behaviors of two boron isotopes, i.e., ^{10}B- and ^{11}B-like behaviors. To quantitatively understand the coupled contributions to each Raman peak observed in the natural BAs and BP, we decompose the Raman intensity contribution among all constitutional atoms (i.e., all isotopes of B, As, or P) based on their eigenvectors. For As and P, a single isotope ^{75}As and ^{31}P dominate the natural abundance, respectively. The contribution of Raman intensity from each isotope is determined following:

$$I^X(\omega) \propto \sum_{s,\mathbf{q}\to 0} W^X_{\mathbf{q}s} \frac{\left|\sum_{j\xi} t_j \frac{(e^j_{\mathbf{q}s})_\xi}{\sqrt{m_j}}\right|^2}{\omega_{\mathbf{q}s}} \delta(\omega - \omega_{\mathbf{q}s}), \tag{9}$$

where X could be ^{10}B, ^{11}B, ^{75}As, or ^{31}P, and $W^X_{\mathbf{q}s}$ is the weighting factor of each isotope:

$$W^X_{\mathbf{q}s} = \frac{\sum_{j\in X,\xi} t_j \frac{(e^j_{\mathbf{q}s})_\xi}{\sqrt{m_j}}}{\sum_{j\xi} t_j \frac{(e^j_{\mathbf{q}s})_\xi}{\sqrt{m_j}}}. \tag{10}$$

As shown in Fig. 3, we quantify the total Raman spectra (black solid curve) from respective contributions by each isotope (color dashed curve): ^{10}B, ^{11}B, ^{75}As, or ^{31}P. A prior naïve understanding is that the high-frequency peak corresponds to the ^{10}B-like mode, and the low-frequency peak corresponds to the ^{11}B-like mode. However, from Fig. 3, all isotopes show nonnegligible contributions to each Raman peak due to the strong coupling between ^{10}B and ^{11}B, as discussed above. The interatomic forces between the atomic pairs in the system affect all isotopes and collectively determine the oscillation frequency. Essentially, in this paper, we indicate that the coupling from two isotope modes plays an important role in reshaping the Raman spectral profile.

Another interesting finding based on our calculations is that a negative contribution to total Raman intensity could exist from a certain isotope mode. For example, for BP in Fig. 3(b), at the low-frequency peak, there is a -3.7% contribution from ^{10}B when the ^{10}B concentration is 20%, which indicates ^{10}B and ^{11}B have opposite directions of eigenvectors based on Eqs. (9) and (10), so that ^{10}B mode destructively contributes to the total Raman intensity. To elucidate further, when the ^{10}B mode originally at the Brillouin zone edge folds back to the Brillouin zone center, it gives a negative contribution to the Raman intensity due to the opposite eigenvector and overlapped frequency compared with the ^{11}B mode at the Brillouin zone center. However, the negative contribution is not obvious for BAs because, in BAs, the optical frequencies at the Brillouin zone edge are far away from the frequencies at the Γ point.

Moreover, we exemplify the power of the *ab initio* approach by high-pressure study. Based on the developed *ab initio* theory, we expect that, under high pressures, a resonance shoulder will appear on the lower-frequency side of the ^{11}B TO peak in naturally abundant BAs. From Eq. (8), the Raman intensity is not only affected by the DOS but also the alignment and magnitude of the eigenvectors. Therefore, this prediction of a new resonance shoulder can be understood by looking at the alignment function of the eigenvectors in a specific direction z, which we define as

$$\eta_z = \left[\sum_j \frac{t_j\left(\mathbf{e}^j_{\mathbf{q}s}\right)_z}{\sqrt{m_j}}\right]^2. \tag{11}$$

The larger value of η_z indicates better alignment on vibration. If the eigenvector directions of each atom are randomly distributed, the positive and negative values of $(\mathbf{e}^j_{\mathbf{q}s})_z$ cancel each other, and then η_z becomes zero. When η_z reaches a peak value, the corresponding phonon modes allow high probability for atoms to have synchronous vibrations, i.e., forming a resonance shoulder in the Raman spectra. Based on the *ab initio* theory, η_z is calculated under varied hydrostatic pressures. As shown in Fig. 4(a), η_z shifts toward higher energy from ambient pressure (yellow) to high pressure (red). In addition, the high pressure reshapes the η_z profile: A local peak for η_z evolves at 815 cm^{-1} under 31.5 GPa [pointed circle, Fig. 4(a)]. For this enhanced eigenvector alignment at 815 cm^{-1} under 31.5 GPa, our *ab initio* calculations [black curve, Fig. 4(b)] predict that an abnormal resonance Raman shoulder will appear at the same position. To verify our prediction, we performed an *in situ* Raman experiment under high-hydrostatic pressure using a diamond anvil cell setup [24,79], as illustrated in Fig. 4(c). A BAs single crystal sample was loaded in the diamond anvil cell [Fig. 4(d)]. In Fig. 4(b), the experimental results (circle) are compared with *ab initio* theory predictions (black curve). The experiment shows an evolved resonance shoulder in the Raman spectra (pointed circle) under high pressure: For example, it appears at 775 cm^{-1} for 22.3 GPa, moving further to 815 cm^{-1} for 31.5 GPa, in good agreement with theory prediction (black curve). The experimental observation of such unique features in high-pressure Raman spectra further verified the modeling accuracy based on *ab initio* theory.

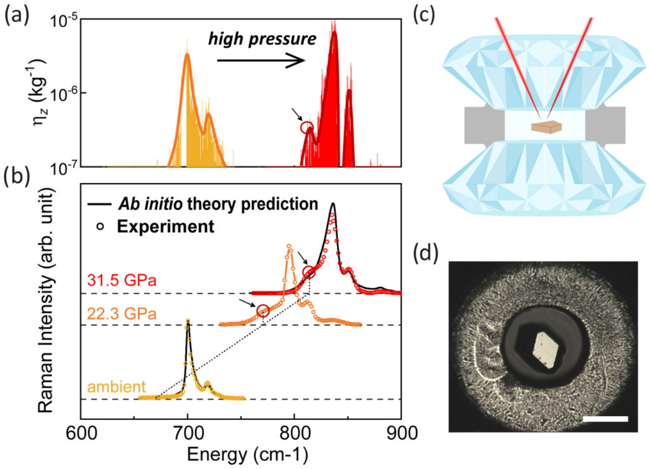

FIG. 4. Abnormal vibrational resonance shoulder for $^{\mathrm{nat}}$BAs under high pressure predicted by *ab initio* theory and verified by experiment. (a) The calculated alignment function η_z at ambient (orange yellow column) and high pressure (red column), predicting an evolving η_z peak at high pressure that facilitate Raman scattering near its shoulder. The profile of η_z is illustrated by solid curves. (b) Comparison between the theory prediction (black curve) and experimental measurement (circle) of Raman spectra under ambient and high pressures, verifying the appearance of a new shoulder (highlighted by red circle and arrow). (c) Experimental setup of diamond anvil cell for *in situ* Raman measurement under high pressure. (d) Image of BAs sample loaded inside the diamond anvil cell. Scale bar is 100 μm. More details regarding high pressure setups and experiments can be found in our recent study in Ref. [24].

In summary, we investigated the vibrational modes in high-thermal-conductivity BAs and BP crystals and quantitively determined the physics origin of the anomalous vibrational modes through the comparison between *ab initio* theory and experiment. We developed *ab initio* calculations based on DFT and a nonperturbative supercell exact diagonalization method to determine the profiles of Raman spectra under varied isotope stoichiometry that show good agreement with experimentally measurements. We found that the dynamic evolution of Raman spectra with isotope stoichiometries can be quantitatively explained by the coupling between all constitutional atoms and the translational symmetry breaking induced by local isotope mass inhomogeneity. By decomposing the Raman insensitivity to each eigenvector of constitutional atoms (e.g., ^{10}B, ^{11}B, ^{75}As, ^{31}P), we clarified that each Raman peak is contributed collectively from all vibrational modes rather than from a single mode, while both constructive and destructive coupling exist. In addition, an abnormal vibrational shoulder is theoretically predicted at high pressure due to breaking of translational symmetry in BAs and experimentally verified by our high-pressure experiment. In this paper, we exemplify the power of combining *ab initio* theory and experiment in exploring new transport phenomena for materials with extreme properties [68,95,96].

Y.H. acknowledges support from the CAREER Award from the National Science Foundation (NSF) under Grant No. DMR-1753393, an Alfred P. Sloan Research Fellowship under Grant No. FG-2019–11788, a NIGMS Research Award under Grant No. R35GM147391, and a Vernroy Makoto Watanabe Excellence in Research Award. For this paper, we used computational and storage services associated with the Hoffman 2 Shared Cluster provided by UCLA Office of Advanced Research Computing's Research Technology Group, and the Bridges-2 at Pittsburgh Supercomputing Center through Allocation No. DMR180111 from Extreme Science and

Engineering Discovery Environment, which was supported by NSF Grant No. 1548562, and from Advanced Cyberinfrastructure Coordination Ecosystem: Services & Support (ACCESS) program, which is supported by NSF Grants No. 2138259, No. 2138286, No. 2138307, No. 2137603, and No. 2138296.

---

[1] N. W. Ashcroft and N. D. Mermin, *Solid State Physics* (Saunders College Publishing, Philadelphia, 1976).

[2] J. M. Ziman, *Principles of the Theory of Solids* (Cambridge University Press, Cambridge, 1972).

[3] J. J. Sakurai, *Modern Quantum Mechanics* (Addison-Wesley Publishing Company, Reading, 1994).

[4] G. D. Mahan, *Many-Particle Physics* (Kluwer, New York, 2000).

[5] H. K. Tang, J. N. Leaw, J. N. B. Rodrigues, I. F. Herbut, P. Sengupta, F. F. Assaad, and S. Adam, The role of electron-electron interactions in two-dimensional Dirac fermions, Science **361**, 570 (2018).

[6] S. Paschen and Q. Si, Quantum phases driven by strong correlations, Nat. Rev. Phys. **3**, 9 (2021).

[7] B. L. Altshuler, Y. Gefen, A. Kamenev, and L. S. Levitov, Quasiparticle lifetime in a finite system: A nonperturbative approach, Phys. Rev. Lett. **78**, 2803 (1997).

[8] P. Dombi, Z. Pápa, J. Vogelsang, S. V. Yalunin, M. Sivis, G. Herink, S. Schäfer, P. Groß, C. Ropers, and C. Lienau, Strong-field nano-optics, Rev. Mod. Phys. **92**, 025003 (2020).

[9] P. Souvatzis, O. Eriksson, M. I. Katsnelson, and S. P. Rudin, Entropy driven stabilization of energetically unstable crystal structures explained from first principles theory, Phys. Rev. Lett. **100**, 095901 (2008).

[10] I. Errea, B. Rousseau, and A. Bergara, Anharmonic stabilization of the high-pressure simple cubic phase of calcium, Phys. Rev. Lett. **106**, 165501 (2011).

[11] T. Tadano and S. Tsuneyuki, Self-consistent phonon calculations of lattice dynamical properties in cubic $SrTiO_3$ with first-principles anharmonic force constants, Phys. Rev. B **92**, 054301 (2015).

[12] J. M. Skelton, L. A. Burton, S. C. Parker, A. Walsh, C.-E. Kim, A. Soon, J. Buckeridge, A. A. Sokol, C. R. A. Catlow, A. Togo *et al.*, Anharmonicity in the high-temperature *Cmcm* phase of SnSe: Soft modes and three-phonon interactions, Phys. Rev. Lett. **117**, 075502 (2016).

[13] J. S. Kang, H. Wu, M. Li, and Y. Hu, Intrinsic low thermal conductivity and phonon renormalization due to strong anharmonicity of single-crystal tin selenide, Nano Lett. **19**, 4941 (2019).

[14] A. Bazavov, D. Toussaint, C. Bernard, J. Laiho, C. DeTar, L. Levkova, M. B. Oktay, S. Gottlieb, U. M. Heller, J. E. Hetrick *et al.*, Nonperturbative QCD simulations with $2+1$ flavors of improved staggered quarks, Rev. Mod. Phys. **82**, 1349 (2010).

[15] R. A. Briceño, J. J. Dudek, and R. D. Young, Scattering processes and resonances from lattice QCD, Rev. Mod. Phys. **90**, 025001 (2018).

[16] M. Q. Huber, Nonperturbative properties of Yang-Mills theories, Phys. Rep. **879**, 1 (2020).

[17] Y. B. Levinson and E. I. Rashba, Electron-phonon and exciton-phonon bound states, Rep. Prog. Phys. **36**, 1499 (1973).

[18] J. Zhu, S. M. Badalyan, and F. M. Peeters, Electron-phonon bound states in graphene in a perpendicular magnetic field, Phys. Rev. Lett. **109**, 256602 (2012).

[19] A. Camacho-Guardian, M. A. Bastarrachea-Magnani, and G. M. Bruun, Mediated interactions and photon bound states in an exciton-polariton mixture, Phys. Rev. Lett. **126**, 017401 (2021).

[20] S. Thébaud, C. A. Polanco, L. Lindsay, and T. Berlijn, Success and breakdown of the T-matrix approximation for phonon-disorder scattering, Phys. Rev. B **102**, 094206 (2020).

[21] S. Baroni, S. de Gironcoli, A. Dal Corso, and P. Giannozzi, Phonons and related crystal properties from density-functional perturbation theory, Rev. Mod. Phys. **73**, 515 (2001).

[22] M. Cardona and M. L. W. Thewalt, Isotope effects on the optical spectra of semiconductors, Rev. Mod. Phys. **77**, 1173 (2005).

[23] G. P. Srivastava, *The Physics of Phonons* (CRC Press, Boca Raton, 1990).

[24] S. Li, Z. Qin, H. Wu, M. Li, M. Kunz, A. Alatas, A. Kavner, and Y. Hu, Anomalous thermal transport under high pressure in boron arsenide, Nature (London) **612**, 459 (2022).

[25] J. S. Kang, H. Wu, and Y. Hu, Thermal properties and phonon spectral characterization of synthetic boron phosphide for high thermal conductivity applications, Nano Lett. **17**, 7507 (2017).

[26] J. S. Kang, M. Li, H. Wu, H. Nguyen, and Y. Hu, Basic physical properties of cubic boron arsenide, Appl. Phys. Lett. **115**, 122103 (2019).

[27] J. S. Kang, M. Li, H. Wu, H. Nguyen, and Y. Hu, Experimental observation of high thermal conductivity in boron arsenide, Science **361**, 575 (2018).

[28] S. Li, Q. Zheng, Y. Lv, X. Liu, X. Wang, P. Y. Huang, D. G. Cahill, and B. Lv, High thermal conductivity in cubic boron arsenide crystals, Science **361**, 579 (2018).

[29] F. Tian, B. Song, X. Chen, N. K. Ravichandran, Y. Lv, K. Chen, S. Sullivan, J. Kim, Y. Zhou, T.-H. Liu *et al.*, Unusual high thermal conductivity in boron arsenide bulk crystals, Science **361**, 582 (2018).

[30] V. G. Hadjiev, M. N. Iliev, B. Lv, Z. F. Ren, and C. W. Chu, Anomalous vibrational properties of cubic boron arsenide, Phys. Rev. B **89**, 024308 (2014).

[31] H. Herchen and M. A. Cappelli, First-order Raman spectrum of diamond at high temperatures, Phys. Rev. B **43**, 11740 (1991).

[32] E. Anastassakis, H. C. Hwang, and C. H. Perry, Temperature dependence of the long-wavelength optical phonons in diamond, Phys. Rev. B **4**, 2493 (1971).

[33] G. Lang, K. Karch, M. Schmitt, P. Pavone, A. P. Mayer, R. K. Wehner, and D. Strauch, Anharmonic line shift and linewidth of the Raman mode in covalent semiconductors, Phys. Rev. B **59**, 6182 (1999).

[34] J. M. Zhang, M. Giehler, A. Göbel, T. Ruf, M. Cardona, E. E. Haller, and K. Itoh, Optical phonons in isotopic Ge studied by Raman scattering, Phys. Rev. B **57**, 1348 (1998).

[35] J. Menéndez and M. Cardona, Temperature dependence of the first-order Raman scattering by phonons in Si, Ge, and α-Sn: Anharmonic effects, Phys. Rev. B **29**, 2051 (1984).

[36] A. Debernardi, S. Baroni, and E. Molinari, Anharmonic phonon lifetimes in semiconductors from density-functional perturbation theory, Phys. Rev. Lett. **75**, 1819 (1995).

[37] M. Cardona and T. Ruf, Phonon self-energies in semiconductors: Anharmonic and isotopic contributions, Solid State Commun. **117**, 201 (2001).

[38] G. Irmer, M. Wenzel, and J. Monecke, The temperature dependence of the LO(T) and TO(T) phonons in GaAs and InP, Phys. Stat. Sol. (b) **195**, 85 (1996).

[39] A. Debernardi, Phonon linewidth in III-V semiconductors from density-functional perturbation theory, Phys. Rev. B **57**, 12847 (1998).

[40] P. Giannozzi, S. de Gironcoli, P. Pavone, and S. Baroni, *Ab initio* calculation of phonon dispersions in semiconductors, Phys. Rev. B **43**, 7231 (1991).

[41] A. Mooradian and G. B. Wright, First order Raman effect in III–V compounds, Solid State Commun. **4**, 431 (1966).

[42] L. Lindsay, D. A. Broido, and T. L. Reinecke, *Ab initio* thermal transport in compound semiconductors, Phys. Rev. B **87**, 165201 (2013).

[43] F. Vallée, Time-resolved investigation of coherent LO-phonon relaxation in III-V semiconductors, Phys. Rev. B **49**, 2460 (1994).

[44] S. Z. Beer, J. F. Jackovitz, D. W. Feldman, and J. H. Parker, Raman and infrared active modes of aluminium phosphide, Phys. Lett. A **26**, 331 (1968).

[45] T. Azuhata, T. Sota, and K. Suzuki, Second-order Raman spectra and lattice dynamics in AlAs, J. Phys.: Condens. Matter **7**, 1949 (1995).

[46] Y. S. Raptis, E. Anastassakis, and G. Kanellis, Second-order Raman scattering in AlSb, Phys. Rev. B **46**, 15801 (1992).

[47] J. Wagner, A. Fischer, W. Braun, and K. Ploog, Resonance effects in first- and second-order Raman scattering from AlAs, Phys. Rev. B **49**, 7295 (1994).

[48] K. Aoki, E. Anastassakis, and M. Cardona, Dependence of Raman frequencies and scattering intensities on pressure in GaSb, InAs, and InSb semiconductors, Phys. Rev. B **30**, 681 (1984).

[49] R. C. C. Leite and J. F. Scott, Resonant surface Raman scattering in direct-gap semiconductors, Phys. Rev. Lett. **22**, 130 (1969).

[50] R. Carles, N. Saint-Cricq, J. B. Renucci, M. A. Renucci, and A. Zwick, Second-order Raman scattering in InAs, Phys. Rev. B **22**, 4804 (1980).

[51] W. Kiefer, W. Richter, and M. Cardona, Second-order Raman scattering in InSb, Phys. Rev. B **12**, 2346 (1975).

[52] K. Karch, P. Pavone, W. Windl, O. Schütt, and D. Strauch, *Ab initio* calculation of structural and lattice-dynamical properties of silicon carbide, Phys. Rev. B **50**, 17054 (1994).

[53] V. Lysenko, D. Barbier, and B. Champagnon, Stress relaxation effect in porous 3C-SiC/Si heterostructure by micro-Raman spectroscopy, Appl. Phys. Lett. **79**, 2366 (2001).

[54] D. W. Feldman, J. H. Parker, W. J. Choyke, and L. Patrick, Phonon dispersion curves by Raman scattering in SiC, polytypes $3C$, $4H$, $6H$, $15R$, and $21R$, Phys. Rev. **173**, 787 (1968).

[55] S. Reich, A. C. Ferrari, R. Arenal, A. Loiseau, I. Bello, and J. Robertson, Resonant Raman scattering in cubic and hexagonal boron nitride, Phys. Rev. B **71**, 205201 (2005).

[56] K. Karch and F. Bechstedt, *Ab initio* lattice dynamics of BN and AlN: Covalent versus ionic forces, Phys. Rev. B **56**, 7404 (1997).

[57] C. Bungaro, K. Rapcewicz, and J. Bernholc, *Ab initio* phonon dispersions of wurtzite AlN, GaN, and InN, Phys. Rev. B **61**, 6720 (2000).

[58] P. Perlin, A. Polian, and T. Suski, Raman-scattering studies of aluminum nitride at high pressure, Phys. Rev. B **47**, 2874 (1993).

[59] O. Brafman, G. Lengyel, S. S. Mitra, P. J. Gielisse, J. N. Plendl, and L. C. Mansur, Raman spectra of AlN, cubic BN and BP, Solid State Commun. **6**, 523 (1968).

[60] L. E. McNeil, M. Grimsditch, and R. H. French, Vibrational spectroscopy of aluminum nitride, J. Am. Ceram. Soc. **76**, 1132 (1993).

[61] L. Filippidis, H. Siegle, A. Hoffmann, C. Thomsen, K. Karch, and F. Bechstedt, Raman frequencies and angular dispersion of polar modes in aluminum nitride and gallium nitride, Phys. Stat. Sol. (b) **198**, 621 (1996).

[62] K. Miwa and A. Fukumoto, First-principles calculation of the structural, electronic, and vibrational properties of gallium nitride and aluminum nitride, Phys. Rev. B **48**, 7897 (1993).

[63] C. Ulrich, A. Debernardi, E. Anastassakis, K. Syassen, and M. Cardona, Raman linewidths of phonons in Si, Ge, and SiC under pressure, Phys. Stat. Sol. (b) **211**, 293 (1999).

[64] X. Yang, T. Feng, J. S. Kang, Y. Hu, J. Li, and X. Ruan, Observation of strong higher-order lattice anharmonicity in Raman and infrared spectra, Phys. Rev. B **101**, 161202(R) (2020).

[65] L. Lindsay, D. A. Broido, and T. L. Reinecke, First-principles determination of ultrahigh thermal conductivity of boron arsenide: A competitor for diamond? Phys. Rev. Lett. **111**, 025901 (2013).

[66] J. S. Kang, M. Li, H. Wu, H. Nguyen, T. Aoki, and Y. Hu, Integration of boron arsenide cooling substrates into gallium nitride devices, Nat. Electron. **4**, 416 (2021).

[67] Y. Cui, Z. Qin, H. Wu, M. Li, and Y. Hu, Flexible thermal interface based on self-assembled boron arsenide for high-performance thermal management, Nat. Commun. **12**, 1284 (2021).

[68] Y. Cui, M. Li, and Y. Hu, Emerging interface materials for electronics thermal management: Experiments, modeling, and new opportunities, J. Mater. Chem. C **8**, 10568 (2020).

[69] V. L. Solozhenko, O. O. Kurakevych, Y. Le Godec, A. V. Kurnosov, and A. R. Oganov, Boron phosphide under pressure: In situ study by Raman scattering and X-ray diffraction, J. Appl. Phys. **116**, 33501 (2014).

[70] Q. Zheng, S. Li, C. Li, Y. Lv, X. Liu, P. Y. Huang, D. A. Broido, B. Lv, and D. G. Cahill, High thermal conductivity in isotopically enriched cubic boron phosphide, Adv. Funct. Mater. **28**, 1805116 (2018).

[71] H. Sun, K. Chen, G. A. Gamage, H. Ziyaee, F. Wang, Y. Wang, V. G. Hadjiev, F. Tian, G. Chen, and Z. Ren, Boron isotope effect on the thermal conductivity of boron arsenide single crystals, Mater. Today Phys. **11**, 100169 (2019).

[72] A. Rai, S. Li, H. Wu, B. Lv, and D. G. Cahill, Effect of isotope disorder on the Raman spectra of cubic boron arsenide, Phys. Rev. Mater. **5**, 013603 (2021).

[73] S. Tamura, Isotope scattering of dispersive phonons in Ge, Phys. Rev. B **27**, 858 (1983).

[74] G. D. Mahan, Effect of atomic isotopes on phonon modes, Phys. Rev. B **100**, 024307 (2019).

[75] P. Dean, The vibrational properties of disordered systems: Numerical studies, Rev. Mod. Phys. **44**, 127 (1972).

[76] M. T. Dove and M. T. Dove, *Introduction to Lattice Dynamics* (Cambridge University Press, Cambridge, 1993).

[77] P. Hohenberg and W. Kohn, Inhomogeneous electron gas, Phys. Rev. **136**, B864 (1964).

[78] W. Kohn and L. J. Sham, Self-consistent equations including exchange and correlation effects, Phys. Rev. **140**, A1133 (1965).

[79] See Supplemental Material at http://link.aps.org/supplemental/10.1103/PhysRevB.108.L140302 for details of computation settings or high pressure measurements.

[80] H. Wu, H. Fan, and Y. Hu, *Ab initio* determination of ultrahigh thermal conductivity in ternary compounds, Phys. Rev. B **103**, L041203 (2021).

[81] H. Fan, H. Wu, L. Lindsay, and Y. Hu, *Ab initio* investigation of single-layer high thermal conductivity boron compounds, Phys. Rev. B **100**, 085420 (2019).

[82] T. Thonhauser, V. R. Cooper, S. Li, A. Puzder, P. Hyldgaard, and D. C. Langreth, Van der Waals density functional: Self-consistent potential and the nature of the van der Waals bond, Phys. Rev. B **76**, 125112 (2007).

[83] K. Lee, É. D. Murray, L. Kong, B. I. Lundqvist, and D. C. Langreth, Higher-accuracy van der Waals density functional, Phys. Rev. B **82**, 081101(R) (2010).

[84] K. Berland, V. R. Cooper, K. Lee, E. Schröder, T. Thonhauser, P. Hyldgaard, and B. I. Lundqvist, Van der Waals forces in density functional theory: A review of the vdW-DF method, Rep. Prog. Phys. **78**, 066501 (2015).

[85] V. R. Cooper, Van der Waals density functional: An appropriate exchange functional, Phys. Rev. B **81**, 161104(R) (2010).

[86] J. Klimeš, D. R. Bowler, and A. Michaelides, Van der Waals density functionals applied to solids, Phys. Rev. B **83**, 195131 (2011).

[87] P. Giannozzi, S. Baroni, N. Bonini, M. Calandra, R. Car, C. Cavazzoni, D. Ceresoli, G. L. Chiarotti, M. Cococcioni, I. Dabo *et al.*, QUANTUM ESPRESSO: A modular and open-source software project for quantum simulations of materials, J. Phys.: Condens. Matter **21**, 395502 (2009).

[88] P. Giannozzi, O. Andreussi, T. Brumme, O. Bunau, M. Buongiorno Nardelli, M. Calandra, R. Car, C. Cavazzoni, D. Ceresoli, M. Cococcioni *et al.*, Advanced capabilities for materials modelling with QUANTUM ESPRESSO, J. Phys.: Condens. Matter **29**, 465901 (2017).

[89] P. Giannozzi, O. Baseggio, P. Bonfà, D. Brunato, R. Car, I. Carnimeo, C. Cavazzoni, S. de Gironcoli, P. Delugas, F. Ferrari Ruffino *et al.*, QUANTUM ESPRESSO toward the exascale, J. Chem. Phys. **152**, 154105 (2020).

[90] T. Tadano, Y. Gohda, and S. Tsuneyuki, Anharmonic force constants extracted from first-principles molecular dynamics: Applications to heat transfer simulations, J. Phys.: Condens. Matter **26**, 225402 (2014).

[91] Y. Wang, J. J. Wang, W. Y. Wang, Z. G. Mei, S. L. Shang, L. Q. Chen, and Z. K. Liu, A mixed-space approach to first-principles calculations of phonon frequencies for polar materials, J. Phys.: Condens. Matter **22**, 202201 (2010).

[92] M. Born and M. Bradburn, The theory of the Raman effect in crystals, in particular rock-salt, Proc. R. Soc. Lond. A **188**, 161 (1947).

[93] W. Hayes and R. Loudon, *Scattering of Light by Crystals* (John Wiley and Sons, New York, 1978).

[94] S. Baroni, S. de Gironcoli, and P. Giannozzi, Phonon dispersions in $\mathrm{Ga}_x\mathrm{Al}_{1-x}\mathrm{As}$ alloys, Phys. Rev. Lett. **65**, 84 (1990).

[95] M. Li, L. Dai, and Y. Hu, Machine learning for harnessing thermal energy: From materials discovery to system optimization, ACS Energy Lett. **7**, 3204 (2022).

[96] Z. Qin, M. Li, J. Flohn, and Y. Hu, Thermal management materials for energy-efficient and sustainable future buildings, Chem. Commun. **57**, 12236 (2021).

Correction: Two terms were missing from Eq. (10) and have been inserted. The previously published Figure 3 contained an erroneous label and an incomplete curve in panel (b) and has been replaced.